

Interplay of complex decay processes after argon $1s$ ionization

R. Guillemin,^{1,2} K. Jänkälä,³ B. Cunha de Miranda,¹ T. Marin,¹ L. Journal,^{1,2} T. Marchenko,^{1,2} O. Travnikova,^{1,2} G. Goldsztejn,¹ I. Ismail,¹ R. Püttner,⁴ D. Céolin,² B. Lassalle-Kaiser,² M. N. Piancastelli,^{1,5} and M. Simon^{1,2}

¹*Sorbonne Universités, UPMC Université Paris 06, CNRS, UMR 7614, Laboratoire de Chimie Physique Matière et Rayonnement, F-75005, Paris, France*

²*Synchrotron SOLEIL, l'Orme des Merisiers, Saint-Aubin, BP 48, 91192 Gif-sur-Yvette Cedex, France*

³*Nano and Molecular Systems Research Unit, University of Oulu, P.O. Box 3000, 90014 Oulu, Finland*

⁴*Fachbereich physik, Freie Universität Berlin, Arnimallee 14, D-14195 Berlin, Germany*

⁵*Department of Physics and Astronomy, Uppsala University, P.O. Box 516, SE-751 20 Uppsala, Sweden*



(Received 13 November 2017; published 23 January 2018)

Complex decay pathways involving radiative and nonradiative relaxation after deep core-level ionization in argon are disentangled by a unique combination of several synchrotron radiation-based spectroscopic techniques. In particular, by comparing the results obtained from electron-ion coincidence, photon-ion coincidence, and x-ray emission measurements, we are able to distinguish the final ionic states produced in the cascade decay involving $K\alpha$ and $K\beta$ radiative decay and final ionic states produced by nonradiative cascade decay. High-resolution Auger electron spectroscopy is then used as a complementary tool to identify the LMM transitions contributing to the cascade decay. *Ab initio* calculations are performed to identify the electronic states involved in the LMM decay.

DOI: [10.1103/PhysRevA.97.013418](https://doi.org/10.1103/PhysRevA.97.013418)

I. INTRODUCTION

Absorption of an x-ray photon by an atom or a molecule promotes an electron from a deep shell to an empty orbital or into the ionization continuum. The resulting electronic state with an inner hole is highly unstable. When such inner vacancies are produced by hard x rays in heavy atoms, electronic relaxation can be accomplished in a variety of ways involving complex multistep cascades [1,2], radiative and nonradiative decays with shakeup and shakeoff of one or more electrons [3], as well as Coster-Kronig transitions, and more exotic pathways such as two-electron one-photon [4] and two-electron one-electron decay [5]. The variety and abundance of possible decay channels can make the interpretation of Auger spectra quite difficult. Deep core-hole states have very short lifetimes, usually on the femtosecond time scale. Consequently, electronic state-lifetime interferences between various pathways leading to the same final states can further complicate the picture [6–11]. Moreover, fluorescence can play a role in the decay of the initial core-hole state, and the deeper the vacancy, the higher the probability of radiative decay compared to the Auger decay [12].

In this study, we report on a joint experimental and theoretical investigation of relaxation cascades after $1s$ photoionization of argon. We show that, while different spectroscopic techniques can certainly give an accurate description of some aspects of such a complex process, our suitable unprecedented combination of several of those is crucial in gathering information on the interplay of all possible pathways, and therefore in deriving a complete picture of the overall phenomenon.

Argon is in industrial processes massively separated from air, inexpensive, safe to manipulate, and the K -shell ionization energy of 3200 eV is easily accessible with an x-ray tube or on modern synchrotron radiation sources. As such, argon has long

been a model system to study phenomena associated with the creation of a deep inner-shell vacancy. An additional appealing feature of argon is that its closed-shell nature significantly simplifies theoretical treatment of the photoionization process. The K -shell ionization of argon was first studied by Carlson and Krause in 1965 using filtered radiation from an x-ray tube [1]. Following this pioneering study, more recent measurements were achieved using synchrotron radiation, with broadband excitation [13,14] and monochromatized radiation [15–17]. The most notable consequence of $1s$ core ionization in argon is the production of highly charged ions up to $7+$ [17]. The mechanism to create highly charged ions after single-photon absorption is in general understood in terms of cascade Auger decay. When an incident photon is absorbed and a $1s$ electron is promoted to an empty orbital or to the continuum, the $1s$ core hole created mainly decays by KLL relaxation in which two electrons from the L shell participate to the decay: one electron fills the hole and the other one is ejected into the continuum. The system is left in a highly unstable double core-hole state L^{-2} . This state will then again decay preferentially by Auger relaxation, involving the emission of more electrons. This cascading process leads to the production of ionic charges ranging from $1+$ to $7+$, Ar^{4+} being the main ion produced with a 46% probability [17].

The role played by fluorescence has been long recognized and has been studied by means of coincidence measurements between Auger electrons and fluorescence x-ray photons [18,19]. The relative weight of the radiative channel in Ar had been estimated between 8% and 14% [2,17,20]. Radiative decay pathways branch into several subchannels [21]. $K\beta$ fluorescence (using Siegbahn notation, KM using IUPAC notation), which is responsible for the formation of Ar^+ after $1s$ ionization, leads to a state with a valence hole with no further energetically allowed decay. $K\alpha$ fluorescence (KL),

on the other hand, leads to a state with one $2p$ hole that can further decay. $K\alpha$ fluorescence followed by LMM Auger decay has been shown to be associated with the formation of Ar^{2+} [17]. Note that creation of this single L^{-1} hole state following $1s$ ionization can only be achieved by $K\alpha$ radiative decay, while KLM Auger decay leads to a $L^{-1}M^{-1}$ two-hole state. Obviously, decay cascades involving fluorescence will lead to lower charge states and different Auger lines compared to purely nonradiative decay channels.

While both Auger electron and ion coincidences [13,14,22] and Auger electron and photon coincidences [18,19] have been used to study cascade decay following argon $1s$ photoionization, no data are available on photon and ion coincidences. It is our aim in this paper to identify ionic final states and Auger lines associated with relaxation pathways involving radiative decay. To achieve this goal, we used coincidence measurements between photoelectron and ion, photon and ion, as well as fluorescence spectroscopy and Auger spectroscopy to clearly identify the contribution of radiative decays to the ion production following argon $1s$ ionization, and to the LMM Auger spectrum involved in the cascade decay of the initial core hole. *Ab initio* calculations of the intermediate and final electronic states were performed, and theoretical spectra are compared to experimental ones.

Our paper is organized as follows. Experimental and theoretical methods are described in Sec. II. In Sec. III, we compare the ion yields obtained in coincidence with photons and photoelectrons after direct $1s$ ionization. Radiative relaxation is discussed in Sec. III A and the experimental and calculated LMM Auger spectra are discussed in Sec. III B. In Sec. IV, a short discussion of the results obtained after resonant excitation to the $4p$ and $5p$ Rydberg states is provided.

II. METHODS

A. Experiment

Photon-ion and photoelectron-ion coincidence measurements were performed on the LUCIA [23] and GALAXIES [24] beamlines at the French national synchrotron facility SOLEIL. The data were collected using a double momentum spectrometer [25]. In our experimental geometry, the photon beam crosses a cold supersonic jet of argon at a right angle, forming an interaction volume of approximately $0.1 \times 1 \times 2 \text{ mm}^3$. In its original configuration, the setup is designed to measure electrons and ions in coincidence, using a static electric field to separate and accelerate charged particles towards two opposing time-of-flight spectrometers positioned perpendicularly to the photon beam and atomic jet. The time of flight and impact positions of the electrons and ions detected in coincidence are recorded, and used to derive the three components of the momentum vector of each particle. The efficiency of this recently developed setup has been validated by a series of successful experiments that provided a quantity of new results such as the electronic relaxation of core-ionized argon [17], post-collision interaction [26,27], and molecular-frame photoelectron angular distributions [28,29]. In this study, we did not take advantage of the full momentum measurement capability of the apparatus. Only the time of flight of the ions was used to produce ion mass spectra. A 20 V cm^{-1} extraction

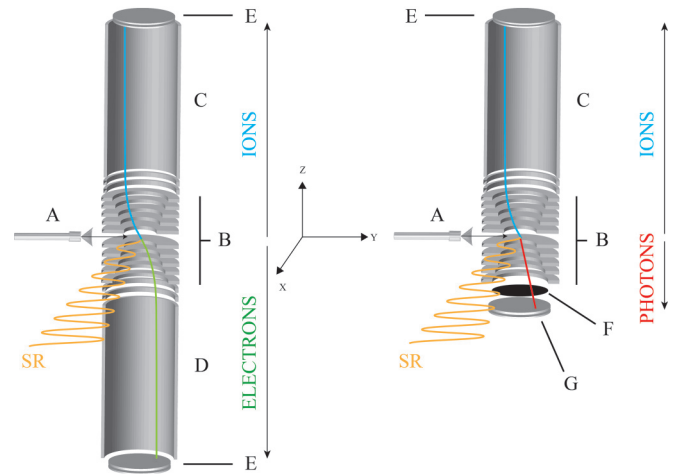


FIG. 1. Schematics of the coincidence setups. Left: electron-ion coincidence setup. A: molecular jet; B: electrostatic lenses; C: ion time-of-flight spectrometer; D: electron time-of-flight spectrometer; E: 80-mm microchannel plates; SR: synchrotron radiation. Right: photon-ion coincidence setup. F: aluminized-mylar filter; G: CsI-coated microchannel plates. See text for details.

electric field was used to collect all electrons and ions with a kinetic energy of 20 eV or less within a 4π solid angle. Measurements were performed at a photon energy 6 eV above the $1s$ ionization threshold (3206.26 eV [15]), and on top of the $1s \rightarrow 4p$ transition at 3203.5 eV, and $1s \rightarrow 5p$ transition at 3205.1 eV. The photon energy above threshold was chosen to minimize the effects of post-collision interaction and electron recapture on the ion rates [17,30], while photoelectrons are still slow enough so they can be efficiently measured within a 4π solid angle using a low extraction field.

To detect photons instead of electrons, the accelerating lens system was kept in place to preserve the homogeneity of the electric field for the ions, but one time-of-flight spectrometer was removed and replaced with a $0.5\text{-}\mu\text{m}$ -thick aluminized-mylar filter (see Fig. 1). A set of microchannel plates coated with cesium iodide was used for improved photon detection efficiency. Although the detection efficiency stays rather poor with this setup (estimated to 5%), microchannel plate's signal is fast and particularly well adapted for coincidence measurements. Aluminized mylar provides an excellent filter blocking all charged particles and is essentially transparent to all photons with energies above 2000 eV ($>0.97\%$ transmission above 2000 eV and 0.99% transmission between 2950 and 3250 eV). On the opposite side, the setup remained unchanged. Coincidence events were digitalized with a time-to-digital converter triggered by the arrival of a photon on the coated channel plates and gated on the time of flight of the slowest ion, namely, Ar^+ .

The experimental measurements of high-resolution Auger spectra were carried out on the GALAXIES beamline, using the HAXPES end station dedicated to hard x-ray photoelectron spectroscopy [31]. Briefly, linearly polarized light is provided by a U20 undulator and monochromatized by a Si(111) double-crystal arrangement. Electrons are analyzed by a large acceptance angle EW4000 Scienta hemispherical analyzer, which lens axis is set parallel to the polarization axis of the synchrotron radiation. The unique capabilities of this apparatus

for high-energy high-resolution spectroscopy allow revealing fine details of relaxation dynamics and have already provided a novel insight in the processes taking place after deep-core level ionization [32–35]. In this study, the electron spectrometer resolution was estimated to be ~ 180 meV at 100-eV pass energy and the photon bandwidth delivered by the beamline is 350 meV at 3200-eV photon energy. Auger decay spectra were recorded on top of the $1s \rightarrow 4p$ and $1s \rightarrow 5p$ transitions, and 20 eV above the ionization threshold, high enough to minimize the effect of post-collision interaction on the Auger lines [30], and low enough to neglect recoil effect such as measured on neon at high photon energy [32].

B. Theoretical calculations

The atomic-state calculations were carried out using the GRASP2K code [36,37] with the RELCI extension [38]. Standard GRASP2K calculations utilize the multiconfiguration Dirac-Fock model where the atomic-state functions are formed as linear combinations of jj -coupled configuration state functions (CSFs) of the same total angular momentum and parity, and are optimized on the basis of the many-electron Dirac-Coulomb Hamiltonian. The CSFs are constructed from antisymmetrized products of a common set of orthonormal radial orbitals. Further relativistic corrections to the electron-electron interaction can be added later in a second step by diagonalizing the Dirac-Coulomb-Breit Hamiltonian matrix.

For simulating the ion yields and the measured Auger spectra, ionic states up to Ar^{+7} were calculated. Calculations of states were performed within the average level scheme where the radial orbitals of an ionic step are optimized to represent all states with equal weights. Cascades that started from the $\text{Ar}(2p^{-1})$ states were first calculated using only the main configurations, meaning configurations constructed using the orbitals of the ground-state configuration $1s^2 2s^2 2p^6 3s^2 3p^6$ of Ar plus $4p$ or $5p$ orbital in the $1s \rightarrow np$ excited cases. These calculations were, however, deemed unsuccessful because, for example, if the $\text{Ar}(2p^{-1}nl)$ states decay via Auger to $(3s3p)^{-2}nl$ states only a single level is above Ar^{+3} states and no Ar^{+3} state is above the Ar^{+4} states. The calculations were therefore extended to include all configurations having single and double excitations to $3d$ and $4s$ orbitals. The number of configurations was limited by including only configurations that can directly interact with the main configurations via Dirac-Coulomb Hamiltonian. Cascades that started from the $\text{Ar}(1s^{-1})$, $\text{Ar}(1s^{-1}4p)$, or $\text{Ar}(1s^{-1}5p)$ states were calculated using only orbitals present in the ground-state configuration, plus $4p$ or $5p$ orbitals in the case of excited states. This limitation was necessary because, especially in the middle of the decay cascade, if more orbitals are included, the number of Auger transition matrix elements that need to be calculated rises to several millions. At the selected level, reproducing the full cascade required calculation of about 25 000 transitions in the $\text{Ar}(1s^{-1})$ case. In contrast, the total amount of Auger transitions required in the $(1s^{-1}4p)$ and $(1s^{-1}5p)$ cases was almost a million.

The Auger transition probabilities were calculated using the AUGER component of the RATIP package [39], that was modified to allow parallelized computation. The radiative transitions were modeled using the REOS program [40]. The AUGER

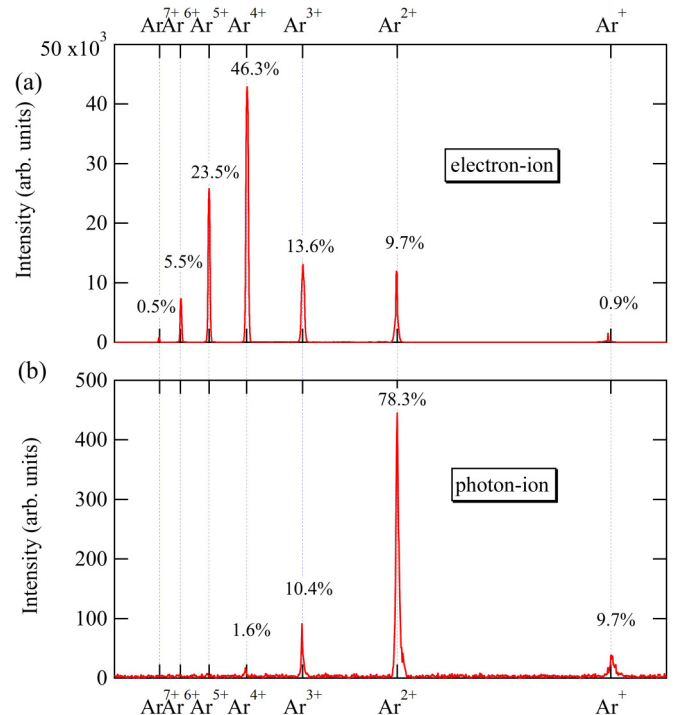


FIG. 2. Coincidence spectra measured 6 eV above the argon $1s$ ionization threshold: (a) photoelectron-ion coincidences, (b) photon-ion coincidences.

program can model only single Auger electron emission, meaning that higher-order processes such as direct double and triple Auger decays were not included in the calculations. This is not an issue when modeling normal Auger spectra because the excess energy is shared continuously in higher-order Auger processes. It, however, gives a small error to the simulation of ion yields.

III. DIRECT IONIZATION

Figure 2 shows the ion spectra obtained at a photon energy of 6 eV above ionization threshold by coincidence measurements between ions and photoelectrons [Fig. 2(a)] and between ions and photons [Fig. 2(b)]. The measurement of all ions produced in coincidence with $1s$ photoelectrons filters out ions produced by x-ray absorption from higher electronic shells. This means that all ions measured in Fig. 2(a) are produced by the decay of a $1s$ core hole, independently of the decay channel. Therefore, Fig. 2(a) also includes all the ions produced via decay channels that involve emission of a photon at one step of the cascade. By contrast [Fig. 2(b)], the coincidence spectrum shows only ions produced via decay involving at least one $K\alpha$ or $K\beta$ photon. Under our experimental conditions, the time it takes for the ion to travel from the interaction region to the detector is typically $12.5 \mu\text{s}$ for Ar^+ and $4.7 \mu\text{s}$ for Ar^{7+} . Thus, the time of flight of the ion is much longer than the Auger cascade. As an example, the effective lifetime is 6.6 fs for the production of Ar^{2+} [17]. Therefore, in our measurements, the coincidence between an electron or a photon is always with the final ionic product of the decay cascade. For both measurements, the ion branching ratios are given in the figure and reported

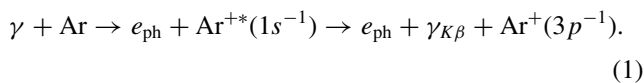
TABLE I. Experimental and calculated ion branching ratios for photoelectron-ion and photon-ion coincidences. The photoelectron-ion branching ratios include all decay channels. The photon-ion branching ratios include only cascade decays involving either $K\alpha$ or $K\beta$ emission.

	Photoelectron-ion		Photon-ion	
	Expt.	Calc.	Expt.	Calc.
Ar ⁺	0.9 ± 0.1%	1.21	9.7 ± 0.2%	10.40
Ar ²⁺	9.7 ± 0.1%	10.66	78.3 ± 0.6%	76.80
Ar ³⁺	13.6 ± 0.1%	11.23	10.4 ± 0.2%	12.70
Ar ⁴⁺	46.3 ± 0.2%	53.49	1.6 ± 0.1%	0.12
Ar ⁵⁺	23.5 ± 0.1%	17.12		
Ar ⁶⁺	5.5 ± 0.1%	6.29		
Ar ⁷⁺	0.5 ± 0.1%	0.01		

in Table I. Comparison of the two spectra shows as can be expected that ion production associated with radiative decay leads to lower charge states. Whereas the main ion produced after core $1s$ ionization in argon is Ar⁴⁺, with a branching ratio of 46.3%, ion production via radiative decay leads mainly to Ar²⁺, with a branching ratio of 78.3%. Our calculated branching ratios, also summarized in Table I, are in good agreement with the measured branching ratios, except for the higher charges which are found with a much lower probability in the calculations in both cases. This discrepancy essentially comes from the difficulty to account for all the electronic states involved in complex decay cascades since calculations are intrinsically limited by the size of the configuration sets used to keep the calculation time reasonable. In addition, higher-order processes such as double and triple Auger decay were not included in the simulations.

A. Radiative decay

During $1s$ ionization, a photoelectron is emitted to the continuum leaving a singly charged ion with a $1s$ vacancy that we denote as Ar^{+(1s⁻¹)}. Two radiative channels are available to the system, namely, $K\beta$ and $K\alpha$ decays. Using ion recoil analysis and post-collision distortion of the photoelectron lines, we already gave in two previous publications a tentative interpretation of the decay channels for the lower charge states [17,26]. Notably, we estimated that radiative decay represents 10.6% of all decay channels after argon $1s$ core ionization [17]. This value comes from the observed branching ratios of 0.9% of Ar⁺ and 9.7% of Ar²⁺. Indeed, these two ions can only be produced above threshold via decay channels involving radiative decay, with the exception of a weak KMM Auger decay in the case of Ar²⁺. In $K\beta$ decay, a valence electron fills the $1s$ decay and no further electronic decay is energetically possible (further neutral decay can involve the emission of a low-energy photon). $K\beta$ decay therefore leads to the production of Ar⁺. This process can be written as



In $K\alpha$ decay, one electron from the $2p$ shell fills the $1s$ vacancy, leaving a singly charged ion with a $2p$ vacancy,

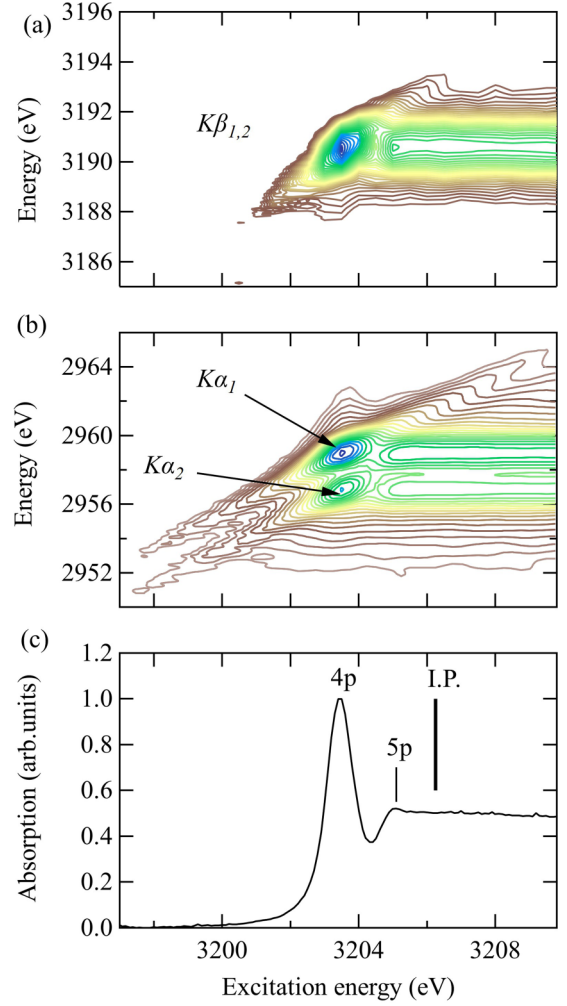


FIG. 3. 2D fluorescence map of argon around the $1s$ ionization threshold. (a) $K\beta$ emission and (b) $K\alpha$ emission. Both maps show the emission intensity and emission energy as a function of excitation energy. (c) Corresponding absorption spectrum. See [21] for details. The positions of the $4p$ and $5p$ resonances, and the ionization threshold (I.P.) are indicated by vertical lines.

Ar^{+(2p⁻¹)}, that can undergo further decay. Based on the recoil of the associated ion, we were able to identify the second step of this cascade as the nonradiative decay of the $2p$ hole via emission of a LMM Auger electron [17]:

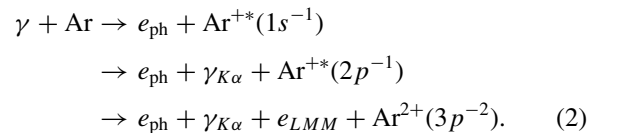


Figure 3 shows the recorded $K\beta$ and $K\alpha$ radiative decay in argon following excitation around the $1s$ ionization threshold. Data are taken from a previous publication [21], and are shown as two-dimensional (2D) maps as a function of excitation energy. $K\beta$ decay is identified in Fig. 3(a) as corresponding to the removal of $3p$ electron. The two spin-orbit $1s^{-1} \rightarrow 3p_{3/2}^{-1}$ and $1s^{-1} \rightarrow 3p_{1/2}^{-1}$ components are separated by only 0.2 eV and merge into a single line in the moderated-resolution spectrum. The two emission lines observed in $K\alpha$ decay correspond to

$1s^{-1} \rightarrow 2p_{3/2}^{-1}$ and $1s^{-1} \rightarrow 2p_{1/2}^{-1}$ transitions separated by 2.2 eV due to spin-orbit interaction. They are respectively labeled $K\alpha_1$ and $K\alpha_2$ in Fig. 3(b). Figure 3(c) shows the absorption spectrum of argon around the $1s$ ionization threshold and the position of the $1s \rightarrow 4p$ and $1s \rightarrow 5p$ resonances below threshold.

As discussed above, in process 1, $K\beta$ decay leads solely to the production of the singly charged ion, and $\gamma_{K\beta}$ is the fluorescence photon detected in coincidence with Ar^+ in Fig. 2(b). This channel has a measured branching ratio of 9.7% of all ions associated with a radiative decay. It should be noted that $K\alpha$ decay to a $2p^{-1}$ core-hole state followed by a secondary radiative decay to a singly charged $3s^{-1}$ state also lead to the creation of Ar^+ but is at least two orders of magnitudes lower than $K\beta$ decay [20,41]. In process 2, $K\alpha$ decay leads to the production of the doubly charged ion, and $\gamma_{K\alpha}$ is the fluorescence photon detected in coincidence with Ar^{2+} in Fig. 2(b), and e_{LMM} is the second-step Auger electron. Although dominant, this channel is not the only pathway leading to the formation of the doubly charged ion. Ar^{2+} can also be produced through KMM nonradiative decay [22,26], which contributes to the partial yield in Fig. 2(a). Because $K\alpha$ decay produces an intermediate state with a single $2p$ hole, the subsequent decay channels should be identical to the decay observed after L -shell ionization. Notably, in process 2, we have written a final ionic state with two holes in the $3p$ outer shell, $\text{Ar}^{2+}(3p^{-2})$. To account for the production of Ar^{3+} and Ar^{4+} in Fig. 2(b), more complex pathways have to be included.

Previous ion yield measurements indicate a probability of forming Ar^{3+} between 10% [42,43] and 13.4% [44]. These values are in good agreement with the experimental value of 10.4% reported in Table I. The formation of Ar^{3+} requires a double Auger decay that may include cascade Auger decays and direct double decays. Double Auger decay after L -shell ionization in argon was first suggested by the observation of a large energy continuum in the recorded Auger spectrum [45]. The identification of Ar^{3+} states with $(3p^3)$ and $(3s^1 3p^4)$ electronic configurations was later made possible using electron-electron coincidences [46], leading to a branching ratio for the triply charged states of 13%. Using multiple electron coincidence measurements, Lablanquie *et al.* [47] studied in details the Auger decay of the $2p^{-1}$ hole in argon showing that double Auger decay leads to the formation of Ar^{3+} and that $(3p^3)^4S$, 2D , and 2P states are predominantly created as soon as the double Auger threshold is reached, with smaller contributions of $\text{Ar}^{3+}(3s^1 3p^4)$ states and satellite states of $(3p^2 nl)$ configurations. The $(3p^3)$ states are reached by cascade Auger decay, with the emission of a fast Auger electron followed by the emission of a slow Auger electron, with an Ar^{2+} intermediate state of $3p^2 3d^2$ configuration. The $(3s^1 3p^4)$ states are only associated with direct double Auger with the simultaneous emission of two electrons. From this study, double Auger decay was estimated to account for at least 9.1% of all Auger decay after the creation of a $2p$ hole. In their study, Lablanquie *et al.* [47,48] also report the observation of triple Auger decay leading to the production of Ar^{4+} with 0.2% of probability. From photoelectron-ion coincidence spectroscopy, Brünken *et al.* [44] previously reported a probability of 0.3%. These numbers are almost an order of magnitude lower than the experimental value 1.6% found in our study,

and slightly higher than our calculated value of 0.12%. In the present calculations, Ar^{3+} and Ar^{4+} final ionic states are reached via $3d$ and $4s$ singly and doubly excited states in the first and second steps of the Auger cascade. Inclusion of even higher excited states would increase the percentage slightly, but most likely not to the observed experimental value.

B. $L_{2,3}MM$ Auger decay

The branching ratios of the different Auger decay pathways available after $1s$ ionization in argon were calculated long ago by Chen *et al.* [49]. $KL_{2,3}L_{2,3}$ decay dominates largely the decay channels with a 55.3% probability, followed by $KL_1L_{2,3}$ (22.1%), KL_1L_1 (6.88%), $KL_{2,3}M$ (11.4%), and KL_1M (3.6%). LMM Auger electrons are emitted during the second step in a cascade decay process and follow either KLL Auger decay, KLM decay, or $K\alpha$ radiative decay that leads to the creation of a single-hole $2p^{-1}$ state. The ion formation observed in coincidence with fluorescence photons in Fig. 2(b) is associated with cascade Auger following $K\alpha$ decay, and should appear in the $L_{2,3}MM$ spectrum.

Interestingly, in the present case branching ratios (BR) of the first step of the Auger cascade combined with a knowledge of the highest possible ionic state that can be reached by the individual branches give a fairly good qualitative prediction and understanding for the observed ion yield (IY) in Table I. $KL_{2,3}M$ path terminates to Ar^{3+} which has 11.4% BR in comparison to 13.6% IY, $KL_{2,3}L_{2,3}$ path terminates to Ar^{4+} with 55.3% BR in comparison to 46.3% IY, $KL_1L_{2,3}$ and KL_1M terminate to Ar^{5+} with 25.7% BR in comparison to 23.5% IY, and KL_1L_1 terminates mainly to Ar^{6+} with a

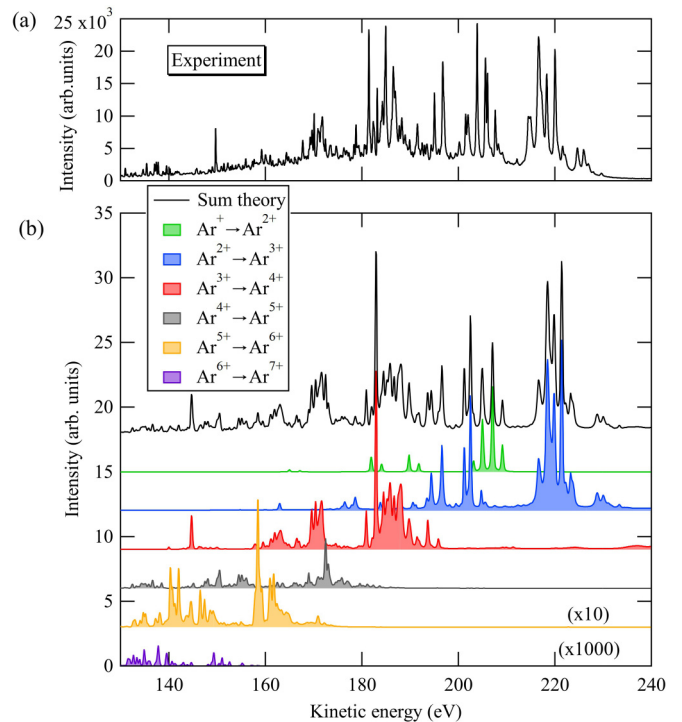


FIG. 4. $L_{2,3}MM$ Auger decay after core $1s$ ionization. (a) Experimental spectrum measured 20 eV above threshold. (b) Total calculated spectrum and partial $\text{Ar}^{n+} \rightarrow \text{Ar}^{m+}$ contributions.

small possibility to reach Ar^{7+} which gives 6.88% BR in comparison to 6% IY. The reason is that for every cascade the most intense decay channels remain open until the termination step. Therefore, the probability divided in the first step is almost completely transferred to the highest possible ionic state, except in the Ar^{7+} case. Obviously, deviations come from contributions of the fluorescence channels and earlier terminations.

Using the HAXPES setup at the GALAXIES beamline, we have measured the $L_{2,3}MM$ spectrum 20 eV above the $1s$ ionization threshold. Figure 4 shows the comparison of the experimental [Fig. 4(a)] and calculated LMM Auger spectra [Fig. 4(b)]. This spectrum illustrates the complexity of the LMM Auger spectrum after $1s$ photoionization in argon where cascade processes dominate the Auger decay. We note that the spectrum measured here is a noncoincident spectrum contrary to the spectra recorded in coincidence with $K\alpha$ photons by Arp *et al.* [18,19]. Therefore, it includes all decay cascades involving radiative and nonradiative pathways. It is, however, possible to disentangle the different contributions with help of theory. Using broadband excitation (where all K , L_1 , and $L_{2,3}$ shells are directly ionized), ion-Auger electron coincidence measurements, and relativistic calculations, von Busch

et al. [14] tentatively provided a complete assignment of the spectator satellites observed in the LMM spectrum of argon corresponding to the transitions to the lower ionic states (up to Ar^{4+}). The purpose of this paper is not to detail all the multitude of individual transitions calculated and resulting spectroscopic terms, therefore, we describe the transitions solely in terms of atomic configuration for the sake of simplicity and clarity, and we include all transitions up to Ar^{7+} .

Our calculated decay spectrum shown in Fig. 4(b) includes Auger transitions between different ionic states that fall into the 120–240 eV kinetic energy range. Both the experimental and calculated spectra are very similar to the $L_{2,3}MM$ spectra we obtained for HCl [50], and we can distinguish in the spectrum transitions we can associate to various decay process. To present our results in a form relevant to our discussion, we regroup the contributions of the many electronic states in terms of transitions between ionic states, i.e., for instance we group together all the transitions from a Ar^{1+} ionic state to a Ar^{2+} ionic state. These groups represent the subspectra shown in Fig. 4(b) and they are shown in detail in Figs. 4 to 7. The partial $L_{2,3}MM$ Auger spectra obtained allow us to clarify the relaxation pathways leading to the ion production measured in Fig. 2. The transitions identified are detailed in Table II. However, it is important to recognize that not all ion production channels are associated with Auger transitions observed in this energy range.

TABLE II. Electronic configurations of initial and final electronic states in the calculated $L_{2,3}MM$ Auger decay after argon $1s$ core ionization.

Transition	Initial configuration	Final configuration	Kinetic energy (eV)
$\text{Ar}^+ \rightarrow \text{Ar}^{2+}$	$2p^5$	$3p^4$	202–210
	$2p^5$	$3s^1 3p^5$	180–194
	$2p^5$	$3s^0$	164–168
$\text{Ar}^{2+} \rightarrow \text{Ar}^{3+}$	$2p^4$	$2p^5 3p^4$	215–235
	$2p^5 3p^5$	$3p^3$	198–208
	$2p^4$	$2p^5 3s^1 3p^5$	190–198
	$2p^5 3p^5$	$3s^1 3p^4$	182–190
	$2p^4$	$2p^5 3s^0$	172–182
$\text{Ar}^{3+} \rightarrow \text{Ar}^{4+}$	$2p^5 3p^5$	$3s^0 3p^5$	159–164
	$2s^1 3p^4$	$3s^1 3p^3$	230–240
	$2s^1 3p^4$	$3s^0 3p^4$	215–230
	$2s^1 2p^5 3p^5$	$2s^1 3p^3$	200–215
	$2p^5 3p^4$	$3p^2$	178–197
	$2p^5 3p^4$	$3s^1 3p^3$	155–178
$\text{Ar}^{4+} \rightarrow \text{Ar}^{5+}$	$2p^5 3p^4$	$3s^0 3p^4$	139–153
	$2p^5 3s^1 3p^4$	$3s^1 3p^2$	168–190
	$2p^5 3p^3$	$3s^1 3p^2$	158–168
	$2p^5 3s^1 3p^4$	$3s^0 3p^3$	140–158
$\text{Ar}^{5+} \rightarrow \text{Ar}^{6+}$	$2p^5 3p^3$	$3s^0 3p^3$	130–140
	$2p^5 3s^1 3p^3$	$3s^1 3p^1$	160–180
	$2p^5 3p^2$	$3s^2$	157–160
$\text{Ar}^{6+} \rightarrow \text{Ar}^{7+}$	$2p^5 3p^2$	$3s^1 3p^1$	136–155
	$2p^5 3s^1 3p^3$	$3s^0 3p^2$	136–155
	$2p^5 3p^2$	$3s^1 3p^1$	132–136
	$2p^5 3s^1 3p^2$	$3s^1 3p^0 + 3s^0 3p^1$	130–160

I. $\text{Ar}^+ \rightarrow \text{Ar}^{2+}$ transitions

The partial Auger spectrum associated with $\text{Ar}^+ \rightarrow \text{Ar}^{2+}$ transitions corresponds to the well-known decay of the $2p^{-1}$ core hole [51] and is displayed in Fig. 5. In the case of an initial $1s$ ionization, these contributions to the LMM Auger spectrum follow the radiative decay of the $1s$ vacancy through

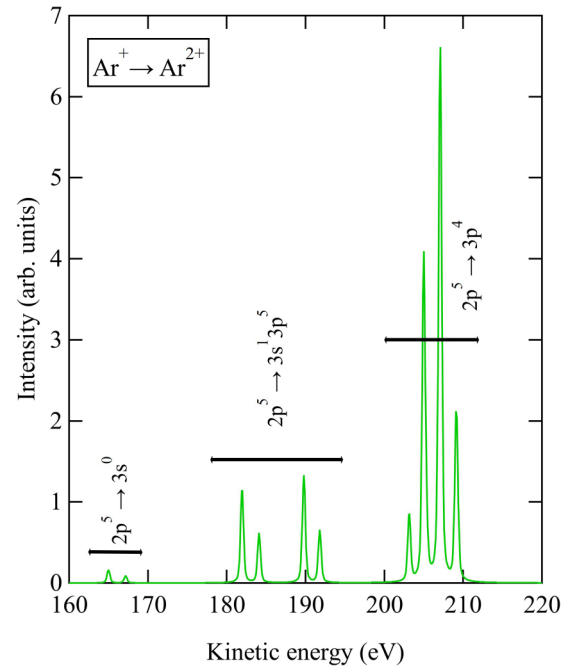


FIG. 5. Partial $\text{Ar}^{1+} \rightarrow \text{Ar}^{2+}$ contribution to the $L_{2,3}MM$ Auger decay after core $1s$ ionization.

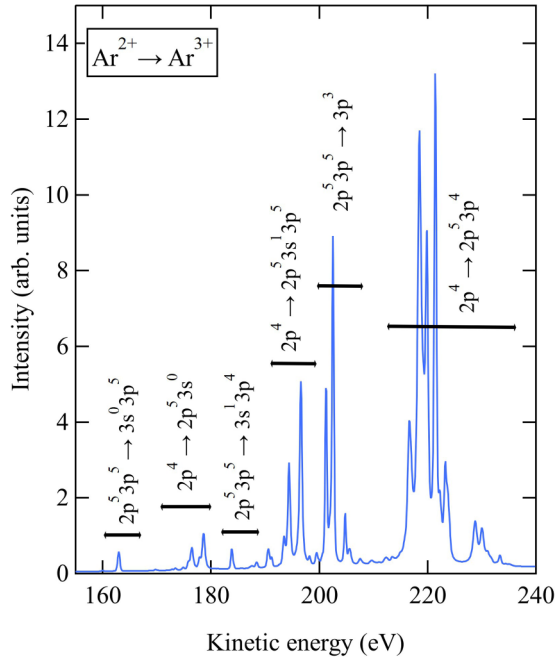


FIG. 6. Partial $\text{Ar}^{2+} \rightarrow \text{Ar}^{3+}$ contribution to the $L_{2,3}MM$ Auger decay after core $1s$ ionization.

$K\alpha$ emission, and the creation of a single $2p$ vacancy, as described above in process 2. The filling of the $2p$ vacancy by $L_{2,3}M_{2,3}M_{2,3}$ decay results in $2p^5 \rightarrow 3p^4$ transitions, leaving the ion with two $3p$ vacancies and leading to 1S_0 , 1D_2 , and $^3P_{0,1,2}$ final states. The 2.2-eV spin-orbit splitting of the $2p$ level into $2p_{3/2}$ and $2p_{1/2}$ core-hole states leads to the partial overlap of these configurations and to the four peaks observed in the 202–210 eV kinetic energy region that was the particular focus of *Arp et al.* [18,19] in their coincidence study. $L_{2,3}M_1M_{2,3}$ decay of the $2p$ vacancy corresponds to $2p^5 \rightarrow 3s^1 3p^5$ transitions which lead to the creation of 1P_1 and $^3P_{0,1,2}$ final states in the 180–194 eV kinetic energy region. Here, the spin-orbit splitting leads to the presence of two groups of two peaks, as observed in this energy region. The last group of peaks observed at lower kinetic energy, 164–168 eV, corresponds to the $L_{2,3}M_1M_1$ decay of the $2p$ vacancy, $2p^5 \rightarrow 3s^0$, leading to two spin-orbit transitions to the 1S_0 final state.

Lablanquie *et al.* [47] observed that the double Auger decay of the $2p^{-1}$ core hole can also produce triply charged Ar^{3+} ions with $(3p^3)$ configurations through a cascade process and $(3s^1 3p^4)$ configurations through direct double Auger decay.

2. $\text{Ar}^{2+} \rightarrow \text{Ar}^{3+}$ transitions

The partial Auger spectrum associated with $\text{Ar}^{2+} \rightarrow \text{Ar}^{3+}$ transitions is shown in Fig. 6. As previously noted by von Busch *et al.* [14], the majority (estimated to 87%) of the initial $KL_{2,3}L_{2,3}$ transitions leads to a $2p^4(^1D_2)$ configuration. Most of the transitions regrouped in the $\text{Ar}^{2+} \rightarrow \text{Ar}^{3+}$ curve in Fig. 6 correspond to the hypersatellites of the $L_{2,3}MM$ decay, i.e., the first step, $2p^{-2} \rightarrow 2p^{-1}$, in the sequential decay of the $2p^{-2}$ double vacancy with an initial $2p^4$ configuration created by KLL decay. The resulting $2p^{-1}$ vacancy undergoes further decay. One can not completely rule out radiative decay

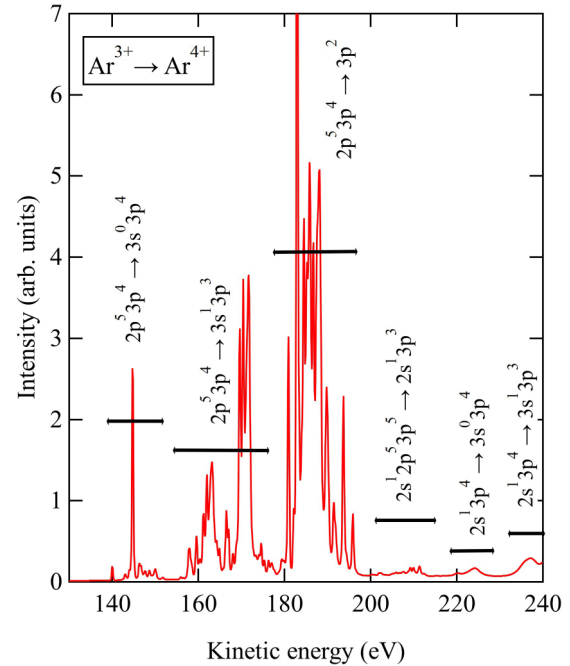


FIG. 7. Partial $\text{Ar}^{3+} \rightarrow \text{Ar}^{4+}$ contribution to the $L_{2,3}MM$ Auger decay after core $1s$ ionization.

of the $2p^{-1}$, however, fluorescence above the $2p$ threshold is expected to be extremely weak [52]. Therefore, these transitions are not associated with the formation of Ar^{3+} and the decay of the remaining $2p^{-1}$ leads almost exclusively to $\text{Ar}^{3+} \rightarrow \text{Ar}^{4+}$ transitions. The corresponding hypersatellite lines are $2p^4 \rightarrow 2p^5 3p^4$ transitions between 215 and 235 eV, $2p^4 \rightarrow 2p^5 3s^1 3p^5$ transitions between 190 and 198 eV, and $2p^4 \rightarrow 2p^5 3s^0$ between 172 and 182 eV.

The formation of Ar^{3+} is mostly associated to the second step of the $KL_{2,3}M_{2,3}$ leading to the configuration $2p^5 3p^5$. These transitions are identified in the spectrum as $2p^5 3p^5 \rightarrow 3p^3$ between 198 and 208 eV, $2p^5 3p^5 \rightarrow 3s^1 3p^4$ between 182 and 190 eV, and $2p^5 3p^5 \rightarrow 3s^0 3p^5$ between 159 and 164 eV.

3. $\text{Ar}^{3+} \rightarrow \text{Ar}^{4+}$ transitions

The curve regrouping the $\text{Ar}^{3+} \rightarrow \text{Ar}^{4+}$ transitions in Fig. 7 is dominated by a large series of transitions lying in the 139–197 eV kinetic energy region. These transitions are the second step, $2p^{-1} \rightarrow 2p^0$, of the sequential decay of the $2p^{-2}$ double vacancy following the $2p^{-2} \rightarrow 2p^{-1}$ LMM decay discussed above (noted $LMM2$ for HCl in [50]). These transitions are identified as follows: $2p^5 3p^4 \rightarrow 3p^2$ between 178 and 197 eV, $2p^5 3p^4 \rightarrow 3s^1 3p^3$ between 155 and 178 eV, and $2p^5 3p^4 \rightarrow 3s^0 3p^4$ between 139 and 153 eV. At higher kinetic energy, we find other minor transitions involving initial states with a $2s$ hole: $2s^1 3p^4 \rightarrow 3s^1 3p^4$ between 230 and 240 eV, $2s^1 3p^4 \rightarrow 3s^0 3p^4$ between 215 and 230 eV, and $2s^1 2p^5 3p^5 \rightarrow 2s^1 3p^3$ between 200 and 215 eV. The latter transition produces a $2s^1 3p^3$ final state that can undergo further Auger decay and lead to the production of Ar^{5+} . All the other transitions have reached a final step in terms of Auger decay and produce Ar^{4+} . As stated above, $KL_{2,3}L_{2,3}$ is the dominant decay channel with a 55.3% probability. Our

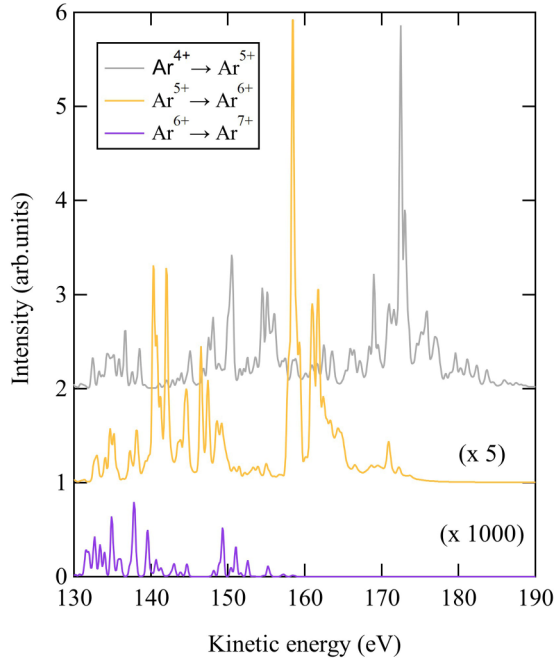


FIG. 8. Partial $\text{Ar}^{4+} \rightarrow \text{Ar}^{5+}$, $\text{Ar}^{5+} \rightarrow \text{Ar}^{6+}$, and $\text{Ar}^{6+} \rightarrow \text{Ar}^{7+}$ contributions to the $L_{2,3}MM$ Auger decay after core $1s$ ionization.

tentative disentanglement of the different contributions to the $L_{2,3}MM$ spectrum shows that most transitions eventually lead to the formation of Ar^{4+} , and explains how this ion is the main ion produced after $1s$ ionization of argon.

4. $\text{Ar}^{4+} \rightarrow \text{Ar}^{5+}$, $\text{Ar}^{5+} \rightarrow \text{Ar}^{6+}$, and $\text{Ar}^{6+} \rightarrow \text{Ar}^{7+}$ transitions

So far, we have only considered LMM decay pathways following $KL_{2,3}L_{2,3}$ which represent the majority of all pathways. However, a remaining 29% is due to first-step $KL_1L_{2,3}$ and KL_1L_1 decays. Therefore, there is a possibility that Auger cascades start from $2s^{-2}$ and $2s^{-1}2p^{-1}$ states, which can end up to higher ionic states. At first these cascades produce electrons in higher kinetic energy region, but subsequent steps can fall into the LMM energy region discussed here. Our theoretical calculations indeed confirm that the low kinetic energy part of the measured LMM spectrum is occupied by weak $\text{Ar}^{4+} \rightarrow \text{Ar}^{5+}$, $\text{Ar}^{5+} \rightarrow \text{Ar}^{6+}$, and $\text{Ar}^{6+} \rightarrow \text{Ar}^{7+}$ transitions. The partial decay spectra calculated for these transitions are displayed in Fig. 8 and corresponding electronic states are summarized in Table II. All these transitions found between 130 and 190 eV involve an initial state with a single $2p$ core hole and several $3s$ and $3p$ vacancies. Only two very weak groups of transitions were found to reach Ar^{7+} , namely, $2p^53s^13p^2 \rightarrow 3s^13p^0$ and $2p^53s^13p^2 \rightarrow 3s^03p^1$ between 130 and 160 eV.

Our calculations show that the cascade decay pathways followed by the system to reach the highest charge states are both long and complex. To illustrate this, we trace the pathways leading to Ar^{7+} . The main configurations of the six-step Auger decay following K -shell ionization can be written as ($1s^2$ orbital is not marked for clarity) $2s^02p^63s^23p^6 \rightarrow 2s^12p^5[3s^23p^5, 3s^13p^6] \rightarrow 2s^22p^4[3s^23p^4, 3s^13p^5] \rightarrow 2s^12p^6[3s^23p^2, 3s^13p^3, 3p^4] \rightarrow$

$2s^22p^5[3s^23p^1, 3s^13p^2] \rightarrow 2s^22p^6[3s^1, 3p^1]$. In particular, we note the $\text{Ar}^{4+} \rightarrow \text{Ar}^{5+}$ step, where the already filled $2s$ orbital appears to lose an electron. It can happen because $2s^22p^4(3s3p)^6$ configurations are indeed higher in energy than $2s^12p^6(3s3p)^4$ configurations, and because $2s^22p^4(3s3p)^6$ configurations mix with $2s^02p^6(3s3p)^6$ and $2s^12p^5(3s3p)^6$ configurations that provide the nonzero parts to the Auger decay matrix elements. As described above, our calculations only take into account single Auger electron processes. However, transitions where two bound electrons move and one electron is emitted into the continuum, such as $2s^22p^4[3s^23p^4, 3s^13p^5] \rightarrow 2s^12p^6[3s^23p^2, 3s^13p^3, 3p^4]$, are included by means of configuration mixing. Indeed, $2s^12p^63s^23p^2$ can mix for instance with $2s^22p^53s^13p^3$, and $2s^22p^43s^23p^4 \rightarrow 2s^22p^53s^13p^3$ is a proper nonzero two-electron Auger matrix element. Therefore, $2s^22p^4[3s^23p^4, 3s^13p^5] \rightarrow 2s^12p^6[3s^23p^2, 3s^13p^3, 3p^4]$ transition becomes nonzero if $2s^22p^53s^13p^3$ configurations are included to the final state. However, it should be noted that the calculated intensity obtained for Ar^{7+} in this way is much lower than the experimental intensity. For reasonable agreement, higher-order processes need to be included. For instance, if one includes shakeups as was done recently in atomic cadmium [53], the intensity of Ar^{7+} would increase.

IV. RESONANT EXCITATION

Under the same experimental conditions, we have measured the ion mass spectra in coincidence with photons at 3203.5 eV, $1s \rightarrow 4p$, and 3205.1 eV, $1s \rightarrow 5p$. The measured ion production for each of these resonances is shown in Fig. 9 and compared to the spectrum measured 6 eV above threshold. The first observation is that the Ar^+ peak dominates the spectrum at the $4p$ resonance, with a branching ratio of 57.2%, followed by Ar^{2+} at 35.2%. At the $5p$ resonance, Ar^+ and Ar^{2+} have about the same intensity with branching ratios of 44.6% and 45.7%, respectively. Table III summarizes the measured and calculated branching ratios for the two resonances compared with the branching ratios obtained above threshold. While a good agreement was found above threshold, our calculations reproduce the experimental findings below threshold only qualitatively. Notably, we find no intensity in the Ar^{4+} channel while a comparable amount is measured above and below threshold. The reason for completely missing the Ar^{4+} channel in the below-threshold cases is that even by including $3d$ and $4s$ excited correlating configurations, all Ar^{+1} levels after the first Auger decay are lower in energy than the lowest Ar^{4+} level. In the above-threshold case, some levels were high enough, bringing some intensity all the way to Ar^{4+} . Including even more configurations would eventually bring some levels high enough also in the below-threshold cases, but the Auger decay rates to these levels would be most likely very small. Therefore, we may conclude that reproducing the experimental results theoretically requires inclusion of double and triple Auger decays in the first step of the cascade.

Compared to the radiative decay above threshold, and in the absence of a photoelectron, $KV_{1,2}$ transitions observed in Fig. 3(a) lead to neutral species. $KL_{1,2}$ decay leads to an excited neutral species with a single hole in the $2p$ shell and an electron in the $4p$ or $5p$ orbital. These highly excited states

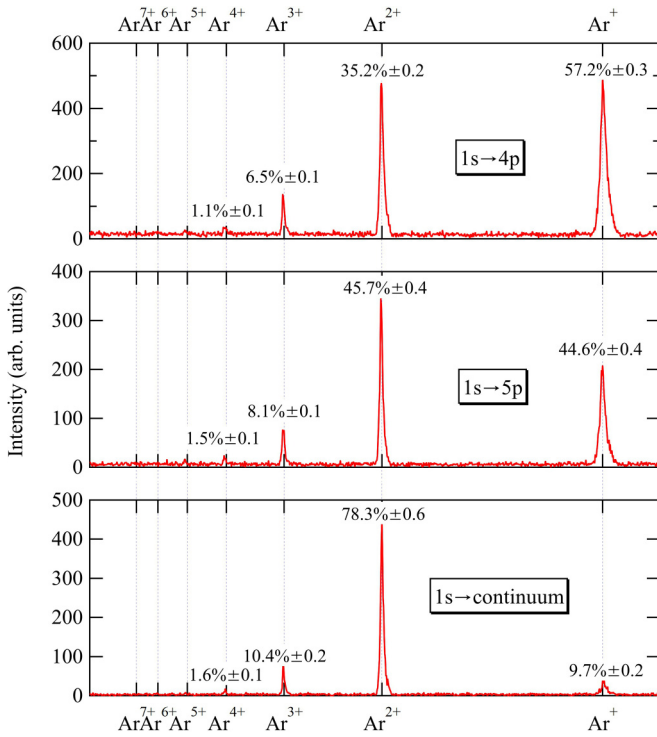


FIG. 9. Comparison of the x-ray photon-ion coincidence spectra measured on top of the $4p$ resonance (top), $5p$ resonance (middle), and 6 eV above the ionization threshold (bottom).

further decay via LMM transitions, leading to the formation of a singly charged ion. Similarly to what was stated above for direct ionization, the only electronic states that can further decay to produce Ar^{2+} are of $3s^0np^1$ configurations. In a simple picture, because $5p$ electrons interact less with the core vacancies than $4p$ electrons, the relative probability for spectator decay, not involving the np excited electron, is higher at the $5p$ resonance than at the $4p$ resonance. $3s^05p^1$ states are therefore formed more efficiently than $3s^04p^1$, and in turn the relative production of Ar^{2+} is increased at the $5p$ resonance. Participant decay at the $4p$ resonance leads to states that cannot further decay, which in turn increases the amount of singly charged ion at the $4p$ resonance. Although the numbers do not agree with the experimental findings, our calculation results reproduced in Table III predict this tendency.

As in the case of direct photoionization, we have calculated the partial contributions to the $L_{2,3}MM$ Auger decay. The experimental spectrum measured at the $4p$ resonance is

TABLE III. Experimental and calculated ion branching ratios for photon-ion coincidences for $1s \rightarrow 4p$ and $1s \rightarrow 5p$ excitations and above-threshold ionization.

	$1s \rightarrow 4p$		$1s \rightarrow 5p$		$1s \rightarrow \epsilon p$	
	Expt.	Calc.	Expt.	Calc.	Expt.	Calc.
Ar^+	$57.2 \pm 0.3\%$	76.30	$44.6 \pm 0.4\%$	69.80	$9.7 \pm 0.2\%$	10.40
Ar^{2+}	$35.2 \pm 0.2\%$	19.10	$45.7 \pm 0.4\%$	27.00	$78.3 \pm 0.6\%$	76.80
Ar^{3+}	$6.5 \pm 0.1\%$	4.60	$8.1 \pm 0.1\%$	3.20	$10.4 \pm 0.2\%$	12.70
Ar^{4+}	$1.1 \pm 0.1\%$	0	$1.5 \pm 0.1\%$	0	$1.6 \pm 0.1\%$	0.12

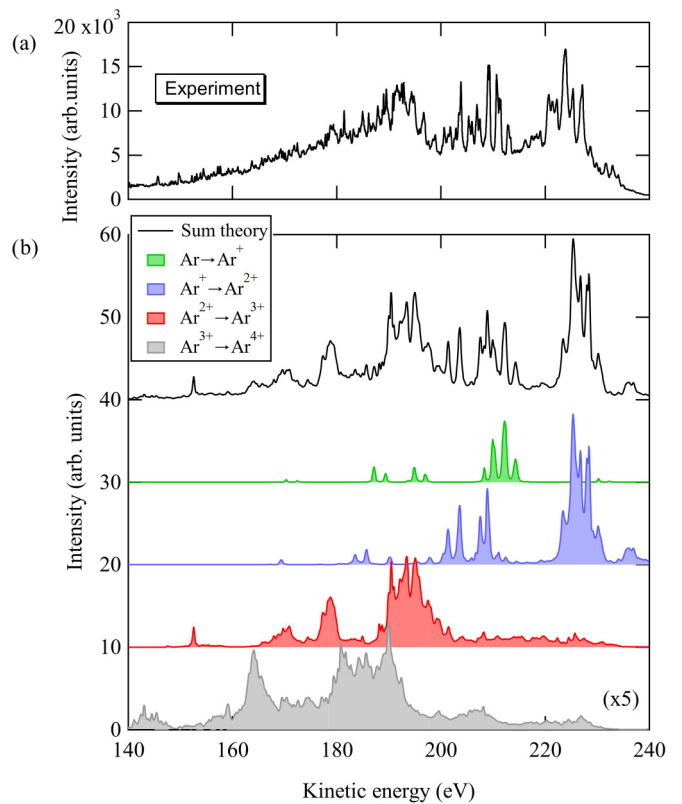


FIG. 10. $L_{2,3}MM$ Auger decay after core $1s \rightarrow 4p$ excitation. (a) Experimental spectrum measured on top of the $4p$ resonance. (b) Total calculated spectrum and partial $\text{Ar}^{n+} \rightarrow \text{Ar}^{m+}$ contributions.

compared to the calculated spectra in Fig. 10. The calculated initial and final states for $\text{Ar}^{n+} \rightarrow \text{Ar}^{m+}$ contributions up to Ar^{4+} are summarized in Table IV. Transitions to higher ionic states were found to be negligible in the $L_{2,3}MM$ Auger energy range. The general features of the spectrum are fairly well reproduced by the calculations. The main difference is absence of a broad spectrum-wide background that starts to increase from about 140 eV kinetic energy, extending all the way to about 240 eV. By comparing Figs. 4 and 10 one can observe that such background is present also in the direct ionization case, but it is considerably more pronounced in the resonant case in Fig. 10. The increase indicates that the background is related to correlation, shakeup, and shakeoff Auger transitions, where the loosely bound $4p$ electron changes its one-electron orbital during the Auger decay. It is also possible that the $4p$ electron is shaken off during the first step of the cascade and the subsequent Auger decays fall into the measured energy region. Due to the enormous number of different possibilities for such transitions during the cascade, the spectrum forms a continuous background which overlaps the main spectrum.

De Gouw *et al.* [54] have studied the resonant Auger decay after $2p_{3/2}$ photoexcitation. However, due to dipole selection rules, photoexcitation below the $2p$ threshold leads to transitions to the $4s$, $3d$, $4d$, and $5d$ unoccupied orbitals, while in our case photoexcitation below the $1s$ threshold leads to occupancy of the $4p$ and $5p$ orbitals. As a result, the measured resonant $L_{2,3}MM$ Auger spectra show different initial and final electronic states. Žitnik *et al.* [55] have measured the resonant

TABLE IV. Electronic configurations of initial and final electronic states in the calculated $L_{2,3}MM$ Auger decay after argon $1s \rightarrow 4p$ excitation.

Transition	Initial configuration	Final configuration	Kinetic energy (eV)
$Ar^0 \rightarrow Ar^+$	$2p^5 4p^1$	$3p^5$	225–235
	$2p^5 4p^1$	$3p^4 4p^1$	203–220
	$2p^5 4p^1$	$3s^1 3p^5 4p^1$	180–200
	$2p^5 4p^1$	$3s^0 4p^1$	167–174
$Ar^+ \rightarrow Ar^{2+}$	$2p^4 4p^1$	$2p^5 3p^4 4p^1$	215.5–240
	$2p^5 3p^5 4p^1$	$3p^3 4p^1$	205.3–215.5
	$2p^4 4p^1$	$2p^5 3s^1 3p^5 4p^1$	199–205.3
	$2p^5 3p^5 4p^1$	$3s^1 3p^4 4p^1$	188–199
	$2p^4 4p^1$	$2p^5 3s^0 4p^1$	180–188
$Ar^{2+} \rightarrow Ar^{3+}$	$2p^5 3p^5 4p^1$	$3s^0 3p^5 4p^1$	160–173
	$2p^5 3p^4 4p^1$	$3p^3$	220–235
	$2p^4 3p^5 4p^1$	$2p^5 3s^1 3p^4 4p^1$	209.5–225
	$2p^4 3s^1 4p^1$	$2p^5 3s^1 3p^4 4p^1$	202.5–219
	$2p^5 3p^4 4p^1$	$3p^2 4p^1$	186–202.5
	$2p^5 3p^4 4p^1$	$3s^1 3p^3 4p^1$	162–186
$Ar^{3+} \rightarrow Ar^{4+}$	$2p^5 3p^4 4p^1$	$3s^0 3p^4 4p^1$	145–160
	$2p^5 3s^0 3p^5 4p^1$	$3s^0 3p^4$	203–235
	$2p^5 3s^1 3p^4 4p^1$	$3s^1 3p^3$	
	$2p^5 3p^3 4p^1$	$3p^2$	
	$2p^5 3s^0 3p^5 4p^1$	$3p^3 4p^1$	185–196
	$2p^5 3s^1 3p^4 4p^1$	$3s^1 3p^2 4p^1$	183.5–187
	$2p^5 3p^3 4p^1$	$3p^1 4p^1$	178.3–183.2
	$2p^5 3s^1 3p^4 4p^1$	$3s^0 3p^3 4p^1$	150–173.8
	$2p^5 3p^3 4p^1$	$3s^1 3p^2 4p^1$	
$2p^5 3p^3 4p^1$	$3s^0 3p^3 4p^1$	134–150	

Auger spectra after $2p$ excitation by electron impact, where excitation to the $4p$ and $5p$ orbitals is possible. However, the

energy resolution obtained with this technique did not allow a clear separation of the different contributions.

In our measurements, spectra and electronic states obtained for the $1s \rightarrow 5p$ excitation were found to be very similar and are not shown in this article. Compared to the results obtained above ionization threshold, no fundamental differences in the electronic configurations are found, apart from the presence of a spectator electron in the $4p$ or $5p$ orbital. It shows, however, that at this stage of the cascade, the decay is almost exclusively spectator decay and a large majority of the final states still have an electron in $4p$ or $5p$ orbital. Only weak transitions to final states with $3p^3$ configurations are found in the $Ar^{2+} \rightarrow Ar^{3+}$ partial Auger spectrum and with $3s^0 3p^4$ and $3p^2$ configurations in $Ar^{3+} \rightarrow Ar^{4+}$.

V. CONCLUSION

Taking advantage of a unique combination of synchrotron radiation-based experimental techniques, we have investigated the main relaxation channels involved in the formation of highly charged ions after core $1s$ ionization of argon. The complementarity of the several different spectroscopic methods we used leads to a better understanding of the fine details of the complex decay pathways involving radiative and nonradiative relaxation after deep core-level ionization. Theoretical calculations were carried out to explain the experimental findings. It was shown that the present-day models are capable of reproducing complex electron and ion spectra arising from up to six-step Auger cascades with fairly good accuracy.

ACKNOWLEDGMENTS

Experiments were performed on the GALAXIES and LUCIA beamlines at SOLEIL Synchrotron, France (Proposal No. 20120122). We are grateful to D. Prieur for technical assistance and to SOLEIL staff for smoothly running the facility.

- [1] T. A. Carlson and M. O. Krause, *Phys. Rev.* **137**, A1655 (1965).
 [2] A. G. Kochur, V. L. Sukhorukov, A. I. Dudenko, and Ph. V. Demekhin, *J. Phys. B: At., Mol. Opt. Phys.* **28**, 387 (1995).
 [3] T. LeBrun, S. H. Southworth, G. B. Armen, M. A. MacDonald, and Y. Azuma, *Phys. Rev. A* **60**, 4667 (1999).
 [4] W. Wölfl, C. Stoller, G. Bonani, M. Suter, and M. Stöckli, *Phys. Rev. Lett.* **35**, 656 (1975).
 [5] M. Žitnik, R. Püttner, G. Goldsztejn, K. Bučar, M. Kavčič, A. Mihelič, T. Marchenko, R. Guillemin, L. Journal, O. Travnikova, D. Céolin, M. N. Piancastelli, and M. Simon, *Phys. Rev. A* **93**, 021401(R) (2016).
 [6] A. Cesar and H. Ågren, *Phys. Rev. A* **45**, 2833 (1992).
 [7] J.-E. Rubensson, M. Neeb, A. Bringer, M. Biermann, and W. Eberhardt, *Chem. Phys. Lett.* **257**, 447 (1996).
 [8] D. Céolin, T. Marchenko, R. Guillemin, L. Journal, R. K. Kushawaha, S. Carniato, S.-M. Huttula, J.-P. Rueff, G. B. Armen, M. N. Piancastelli, and M. Simon, *Phys. Rev. A* **91**, 022502 (2015).
 [9] R. K. Kushawaha, K. Jänkälä, T. Marchenko, G. Goldsztejn, R. Guillemin, L. Journal, D. Céolin, J.-P. Rueff, A. F. Lago, R. Püttner, M. N. Piancastelli, and M. Simon, *Phys. Rev. A* **92**, 013427 (2015).
 [10] G. Goldsztejn, T. Marchenko, D. Céolin, L. Journal, R. Guillemin, J.-P. Rueff, R. K. Kushawaha, R. Püttner, M. N. Piancastelli, and M. Simon, *Phys. Chem. Chem. Phys.* **18**, 15133 (2016).
 [11] G. Goldsztejn, R. Püttner, L. Journal, R. Guillemin, O. Travnikova, R. K. Kushawaha, B. Cunha de Miranda, I. Ismail, D. Céolin, M. N. Piancastelli, M. Simon, and T. Marchenko, *Phys. Rev. A* **95**, 012509 (2017).
 [12] M. O. Krause, *J. Phys. Chem. Ref. Data* **8**, 307 (1979).
 [13] U. Alkemper, J. Doppelfeld, and F. von Busch, *Phys. Rev. A* **56**, 2741 (1997).
 [14] F. von Busch, U. Kuetgens, J. Doppelfeld, and S. Fritzsche, *Phys. Rev. A* **59**, 2030 (1999).

- [15] K. Ueda, E. Shigemasa, Y. Sato, A. Yagishita, M. Ukai, H. Maezawa, T. Hayaishi, and T. Sasaki, *J. Phys. B: At., Mol. Opt. Phys.* **24**, 605 (1991).
- [16] D. V. Morgan, R. J. Bartlett, and M. Sagurton, *Phys. Rev. A* **51**, 2939 (1995).
- [17] R. Guillemin, C. Bomme, T. Marin, L. Journal, T. Marchenko, R. K. Kushawaha, N. Trcera, M. N. Piancastelli, and M. Simon, *Phys. Rev. A* **84**, 063425 (2011).
- [18] U. Arp, J. W. Cooper, T. LeBrun, S. H. Southworth, M. Jung, and M. A. MacDonald, *J. Phys. B: At., Mol. Opt. Phys.* **29**, L837 (1996).
- [19] U. Arp, T. LeBrun, S. H. Southworth, M. A. MacDonald, and M. Jung, *Phys. Rev. A* **55**, 4273 (1997).
- [20] A. Kahoul, A. Abassi, B. Deghfel, and M. Nekkab, *Radiat. Phys. Chem.* **80**, 369 (2011), and references therein.
- [21] R. Guillemin, S. Carniato, L. Journal, W. C. Stolte, T. Marchenko, L. El Khoury, E. Kawerk, M. N. Piancastelli, A. Hudson, D. W. Lindle, and M. Simon, *J. Electron Spectrosc. Relat. Phenom.* **188**, 53 (2013).
- [22] J. C. Levin, C. Biedermann, N. Keller, L. Liljeby, C.-S. O, R. T. Short, I. A. Sellin, and D. W. Lindle, *Phys. Rev. Lett.* **65**, 988 (1990).
- [23] D. Vantelon, N. Trcera, D. Roy, T. Moreno, D. Mailly, S. Guilet, E. Metchalkov, F. Delmotte, B. Lassalle, P. Lagarde, and A.-M. Flank, *J. Synchrotron Radiat.* **23**, 635 (2016).
- [24] J.-P. Rueff, J. M. Ablett, D. Céolin, D. Prieur, Th. Moreno, V. Balédent, B. Lassalle-Kaiser, J. E. Rault, M. Simon, and A. Shukla, *J. Synchrotron Radiat.* **22**, 175 (2015).
- [25] C. Bomme, R. Guillemin, T. Marin, L. Journal, T. Marchenko, D. Dowek, N. Trcera, B. Pilette, A. Avila, H. Ringuenet, R. K. Kushawaha, and M. Simon, *Rev. Sci. Instrum.* **84**, 103104 (2013).
- [26] R. Guillemin, S. Sheinerman, C. Bomme, L. Journal, T. Marin, T. Marchenko, R. K. Kushawaha, N. Trcera, M. N. Piancastelli, and M. Simon, *Phys. Rev. Lett.* **109**, 013001 (2012).
- [27] C. Bomme, R. Guillemin, S. Sheinerman, T. Morin, L. Journal, T. Marchenko, R. K. Kushawaha, N. Trcera, M. N. Piancastelli, and M. Simon, *J. Phys. B: At., Mol. Opt. Phys.* **46**, 215101 (2013).
- [28] C. Bomme, R. Guillemin, T. Marin, L. Journal, T. Marchenko, N. Trcera, R. K. Kushawaha, M. N. Piancastelli, M. Simon, M. Stener, and P. Decleva, *J. Phys. B: At., Mol. Opt. Phys.* **45**, 194005 (2012).
- [29] R. Guillemin, P. Decleva, M. Stener, C. Bomme, T. Marin, L. Journal, T. Marchenko, R. K. Kushawaha, K. Jänkälä, N. Trcera, K. P. Bowen, D. W. Lindle, M. N. Piancastelli, and M. Simon, *Nat. Commun.* **6**, 6166 (2015).
- [30] R. Guillemin, S. Sheinerman, R. Püttner, T. Marchenko, G. Goldsztejn, L. Journal, R. K. Kushawaha, D. Céolin, M. N. Piancastelli, and M. Simon, *Phys. Rev. A* **92**, 012503 (2015).
- [31] D. Céolin, J. M. Ablett, D. Prieur, T. Moreno, J.-P. Rueff, T. Marchenko, L. Journal, R. Guillemin, B. Pilette, T. Marin, and M. Simon, *J. Electron Spectrosc. Relat. Phenom.* **190**, 188 (2013).
- [32] M. Simon, R. Püttner, T. Marchenko, R. Guillemin, R. K. Kushawaha, L. Journal, G. Goldsztejn, M. N. Piancastelli, J. M. Ablett, J.-P. Rueff, and D. Céolin, *Nat. Commun.* **5**, 4069 (2014).
- [33] R. Püttner, G. Goldsztejn, D. Céolin, J.-P. Rueff, T. Moreno, R. K. Kushawaha, T. Marchenko, R. Guillemin, L. Journal, D. W. Lindle, M. N. Piancastelli, and M. Simon, *Phys. Rev. Lett.* **114**, 093001 (2015).
- [34] G. Goldsztejn, T. Marchenko, R. Püttner, L. Journal, R. Guillemin, S. Carniato, P. Selles, O. Travnikova, D. Céolin, A. F. Lago, R. Feifel, P. Lablanquie, M. N. Piancastelli, F. Penent, and M. Simon, *Phys. Rev. Lett.* **117**, 133001 (2016).
- [35] O. Travnikova, N. Sisourat, T. Marchenko, G. Goldsztejn, R. Guillemin, L. Journal, D. Céolin, I. Ismail, A. F. Lago, R. Püttner, M. N. Piancastelli, and M. Simon, *Phys. Rev. Lett.* **118**, 213001 (2017).
- [36] P. Jönsson, X. He, C. Froese Fischer, and I. P. Grant, *Comput. Phys. Commun.* **177**, 597 (2007).
- [37] P. Jönsson, G. Gaigalas, J. Bieroń, C. Froese Fischer, and I. P. Grant, *Comput. Phys. Commun.* **184**, 2197 (2013).
- [38] S. Fritzsche, C. Froese Fischer, and G. Gaigalas, *Comput. Phys. Commun.* **148**, 103 (2002).
- [39] S. Fritzsche, *Comput. Phys. Commun.* **183**, 1525 (2012).
- [40] S. Fritzsche, C. Froese Fischer, and C. Z. Dong, *Comput. Phys. Commun.* **124**, 340 (2000).
- [41] M. H. Chen, B. Crasemann, and H. Mark, *Phys. Rev. A* **24**, 177 (1981).
- [42] T. Hayaishi, E. Murakami, A. Yagishita, F. Koike, Y. Morioka, and J. E. Hansen, *J. Phys. B: At., Mol. Opt. Phys.* **21**, 3203 (1988).
- [43] N. Saito and I. H. Suzuki, *J. Phys. Soc. Jpn.* **66**, 1979 (1997).
- [44] S. Brünken, Ch. Gerth, B. Kanngießer, T. Luhmann, M. Richter, and P. Zimmermann, *Phys. Rev. A* **65**, 042708 (2002).
- [45] T. A. Carlson and M. O. Krause, *Phys. Rev. Lett.* **17**, 1079 (1966).
- [46] J. Viefhaus, S. Cvejanović, B. Langer, T. Lischke, G. Prümper, D. Rolles, A. V. Golovin, A. N. Grum-Grzhimailo, N. M. Kabachnik, and U. Becker, *Phys. Rev. Lett.* **92**, 083001 (2004).
- [47] P. Lablanquie, L. Andric, J. Palaudoux, U. Becker, M. Braune, J. Viefhaus, J. H. D. Eland, and F. Penant, *J. Electron Spectrosc. Relat. Phenom.* **156-158**, 51 (2007).
- [48] P. Lablanquie, M. A. Khalal, L. Andric, J. Palaudoux, F. Penent, J.-M. Bizau, D. Cubaynes, K. Jänkälä, Y. Hikosaka, K. Ito, K. Bučar, and M. Žitnik, *J. Electron Spectrosc. Relat. Phenom.* **220**, 125 (2017).
- [49] M. H. Chen, B. Crasemann, and H. Mark, *At. Data Nucl. Data Tables* **24**, 13 (1979).
- [50] O. Travnikova, T. Marchenko, G. Goldsztejn, K. Jänkälä, N. Sisourat, S. Carniato, R. Guillemin, L. Journal, D. Céolin, R. Püttner, H. Iwayama, E. Shigemasa, M. N. Piancastelli, and M. Simon, *Phys. Rev. Lett.* **116**, 213001 (2016).
- [51] H. Pulkkinen, S. Aksela, O.-P. Sairanen, A. Hiltunen, and H. Aksela, *J. Phys. B: At., Mol. Opt. Phys.* **29**, 3033 (1996).
- [52] J. A. R. Samson, Y. Lu, and W. C. Stolte, *Phys. Rev. A* **56**, R2530(R) (1997).
- [53] R. Beerwerth and S. Fritzsche, *Eur. Phys. J. D* **71**, 253 (2017).
- [54] J. A. de Gouw, J. van Eck, A. C. Peters, J. van der Weg, and H. G. M. Heideman, *J. Phys. B: At., Mol. Opt. Phys.* **28**, 2127 (1995).
- [55] M. Žitnik, M. Kavčič, K. Bučar, B. Paripás, B. Palásthy, and K. Tőkési, *Nucl. Instrum. Methods Phys. Res., Sect. B* **267**, 260 (2009).